B0715

CFD simulation of a reversible solid oxide microtubular cell

María García-Camprubí (1), Miguel Laguna-Bercero (2), Norberto Fueyo (1)

(1) Fluid Mechanics Group (University of Zaragoza) and LIFTEC (CSIC);
C/ María de Luna 3, 50.018, Zaragoza, Spain.

(2) Instituto de Ciencia de Materiales de Aragón, ICMA, CSIC-Universidad de Zaragoza;
C/ Pedro Cerbuna 12, 50009, Zaragoza, Spain.

Tel.: +34-976-762-153
Fax: +34-976-761-882
Norberto.Fueyo@unizar.es

Abstract

In this work, the authors introduce a comprehensive model and the corresponding 3D numerical tool for the simulation of reversible micro-tubular solid oxide fuel cells. It is based on a previous in-house model for SOFC [1], to which some new features has been added to extend its applicability to SOEC. The model considers the following physical phenomena: (i) fluid flow through channels and porous media; (ii) multicomponent mass transfer within channels and electrodes; (iii) heat transfer due to conduction, convection and radiation; (iv) charge motion; and (v) electrochemical reaction. The numerical algorithm to solve this mathematical model is implemented in OpenFOAM, an open source CFD toolbox based on the finite-volume method.

The model accurately describes the characteristic curve (J-V) of the performance of a reversible solid oxide fuel cell, in both SOEC and SOFC modes, as shown in the Figure 1, where experimental data [2] (lines) is plotted versus the numerical results (dots).
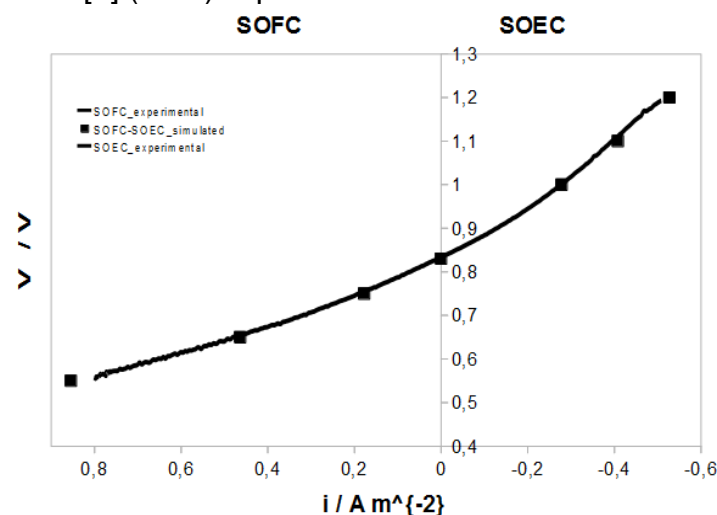
Figure 1: J-V curves, numerical versus experimental data [2].

The model is used to determine the electrochemical-model parameters and to study the physics taking place in both modes of operation. The role of the physical phenomena involved in the performance of a solid-oxide device depending on the operation mode (fuel cell or electrolyser) will be discussed, aiming at providing a basis for the cell optimization.

Introduction

Reversible solid oxide fuel cells, also known as solid oxide regenerative fuel cells (SORFCs), are electrochemical devices that can operate either as an electrolyser (SOEC mode), generating hydrogen if water and electricity are supplied, or as a fuel cell (SOFC mode), consuming hydrogen and producing electricity.

SORFC technology is currently researched by many experimental groups [2,4,5]. However, numerical modeling is scarce in this field. Although there are many numerical works for solid oxide fuel cells (SOFCs) and several for solid oxide electrolyser cells (SOECs), there are hardly any regarding both operating modes simultaneously [6].

In this work, a numerical study of a microtubular anode-supported SORFC is presented. The simulations are performed using a comprehensive numerical tool previously developed by the authors [1,3]. The analysis of the results provide a better understanding of the differences between the SOFC and SOEC operating modes, aiming at helping to the optimization of the cell structure and cell design.

1. Scientific Approach

The numerical study is performed using a comprehensive model that describes the operating principle of SOFCs and SOECs. The model has been described in detail elsewhere [3] and only its relevant features are thus summarised in this section.

The model consists of five submodels, three of which describe the volumetric phenomena taking place within the cell components (channels, electrodes and electrolyte), and the remaining two represent the superficial phenomena, such as the surface-to-surface radiation and the electrochemical reactions.

The channel model describes the fluid flow and the species, mass and heat transfer within the channels; main equations of this model are summarised in Table 1. The electrode model stands for the physics occurring at the fuel and air electrodes, namely: fluid flow, species, mass and heat transfer through a porous medium; the equation set included in this model is shown in Table 2. The electrolyte is an impervious solid where charge and heat transfer are considered, as stated in Table 3.

Table 4 and Table 5 show the algebraic equations used to describe the superficial electrochemical reactions at the electrode-electrolyte interfaces, and the surface-to-surface radiation between the external cell surfaces and the internal furnace surfaces, respectively. For further details see [1,3].

The mathematical model is used to simulate the performance of an in-house fabricated microtubular anode-supported reversible solid oxide fuel cell, shown in Figure 2. The reversible operation of this cell has been experimentally demonstrated [2], and it is numerically studied in this work.

Phenomenon	Equation	Label
Mass conservation	$\nabla \cdot (\rho \vec{v}) = 0$	(1)
Momentum conservation	$\nabla \cdot (\rho \vec{v}\vec{v}) - \nabla \cdot (\mu \nabla \vec{v}) = \nabla \cdot \left\{ \mu (\nabla \vec{v})^T - \dfrac{2}{3}\mu\, tr(\nabla \vec{v})\,\vec{\underline{I}} \right\} - \nabla p$	(2)
Species conservation	$\nabla \cdot (\rho y_\alpha \vec{v}) - \nabla \cdot (\rho D_{\alpha m}\nabla y_\alpha) + \nabla \cdot \left(y_\alpha \rho \sum_{\forall \beta} D_{\beta m}\nabla y_\beta \right) = 0$	(3)
Enthalpy conservation	$\nabla \cdot (\rho C_p \vec{v} T) - \nabla \cdot (\lambda \nabla T) = T\nabla \cdot (C_p \rho \vec{v}) - \nabla \cdot \left(\sum_\alpha (\vec{j}_\alpha h_\alpha) \right)$	(4)

Table 1: Channel model equations

Phenomenon	Equation	Label
Species conservation	$-\nabla \cdot (C_\alpha^* \nabla p_\alpha) + \nabla \cdot (C_\alpha^{p*} p_\alpha) + \nabla \cdot (C_\alpha^{N*} p_\alpha) = S_\alpha$	(5)
Pressure	$p = \displaystyle\sum_{\forall \alpha} p_\alpha$	(6)
Darcy's Law	$\vec{v} = -\dfrac{B_o}{\mu}\nabla p$	(7)
Enthalpy conservation	$\nabla \cdot \left[\sum_\alpha (V_\alpha \vec{N}_\alpha C_{p\alpha}) T \right] - \nabla \cdot (\lambda^{eff}\nabla T) = T\nabla \cdot \left[\sum_\alpha (V_\alpha \vec{N}_\alpha C_{p\alpha}) \right] - \sum_\alpha h_\alpha \nabla \cdot (V_\alpha \vec{N}_\alpha) + {}$ $\qquad\qquad + \varpi + \nabla \cdot \vec{q}_{rad}$ $\varpi_{rc} = i_{rc}(\eta_{act,c} + \eta_{conc,c})$ $\varpi_{ra} = (\Delta H_{r(T=0K)} + nFV_{oc})(\vec{N}_{fuel,ra} \cdot \vec{n}_{ra}) + i_{ra}(\eta_{act,a} + \eta_{conc,a})$	(8)

Table 2: Electrode model equations

Phenomenon	Equation	Label
Charge conservation	$-\nabla \cdot (\tilde{\sigma}\nabla \phi^*) = 0$	(9)
Enthalpy conservation	$-\nabla \cdot (\lambda \nabla T) = \dfrac{i^2}{\tilde{\sigma}} + \nabla \cdot \vec{q}_{rad}$	(10)

Table 3: Electrolyte model equations

Phenomenon	Equation	Label
Cell Voltage	$V = E^o + \dfrac{RT}{2F} \ln\left(\dfrac{p_{H_2} \sqrt{p_{O_2}/p_{ref}}}{p_{H_2O}} \right) - \eta_{ohm} - \left(\eta_{act} + \eta_{con} \right)_a - \left(\eta_{act} + \eta_{con} \right)_c$ $\underbrace{\qquad\qquad\qquad\qquad}_{V_{ocv}}$	(11)
Activation overpotential	$i_{ra} = i_{o,a}\left[\exp\left(\dfrac{\vec{\alpha}_a F \eta_{act,a}}{RT} \right) - \exp\left(\dfrac{-\vec{\alpha}_a F \eta_{act,a}}{RT} \right) \right];$ $\vec{\alpha}_{a,SOEC} = \vec{\alpha}_{a,SOFC} \qquad \vec{\alpha}_{a,SOEC} = \vec{\alpha}_{a,SOFC}$	(12)
	$i_{rc} = i_{o,c}\left[\exp\left(\dfrac{\vec{\alpha}_c F \eta_{act,c}}{RT} \right) - \exp\left(\dfrac{-\vec{\alpha}_c F \eta_{act,c}}{RT} \right) \right];$ $\vec{\alpha}_{c,SOEC} = \vec{\alpha}_{c,SOFC} \qquad \vec{\alpha}_{c,SOEC} = \vec{\alpha}_{c,SOFC}$	(13)
Exchange current density	$i_{o,a} = \gamma_a \left(\dfrac{p_{H_2,ra}}{p_{ref}} \right)^{0.11} \left(\dfrac{p_{H_2O,ra}}{p_{ref}} \right)^{0.67} \exp\left(-\dfrac{E_{act,a}}{RT} \right)$	(14)
	$i_{o,c} = \gamma_c \left(\dfrac{p_{O_2,rc}}{p_{ref}} \right)^{0.25} \exp\left(-\dfrac{E_{act,c}}{RT} \right)$	(15)
Concentration overpotential	$\text{SOFC:} \ \eta_{con,a} = \dfrac{RT}{2F} \ln\left(\dfrac{p_{H_2} p_{H_2O,ra}}{p_{H_2O} p_{H_2,ra}} \right); \quad \text{SOEC:} \ \eta_{con,a} = \dfrac{RT}{2F} \ln\left(\dfrac{p_{H_2,ra} p_{H_2O}}{p_{H_2O,ra} p_{H_2}} \right)$	(16)
	$\text{SOFC:} \ \eta_{con,c} = \dfrac{RT}{2F} \ln\left(\dfrac{\sqrt{p_{O_2}}}{\sqrt{p_{O_2,rc}}} \right); \quad \text{SOEC:} \ \eta_{con,c} = \dfrac{RT}{2F} \ln\left(\dfrac{\sqrt{p_{O_2,rc}}}{\sqrt{p_{O_2}}} \right)$	(17)
Ohmic overpotential	$\text{SOFC:} \ \eta_{ohm} = \phi_{rc}^* - \phi_{ra}^* \qquad\qquad \text{SOEC:} \ \eta_{ohm} = \phi_{ra}^* - \phi_{rc}^*$	(18)

Table 4: Electrochemical model equations

Phenomenon	Equation	Label
Radiative heat flux	$q_{rad,i} = \varepsilon_{rad,i}\left\{ E_{b,i} - \sum_j \left(F_{i-j} E_{b,j} \right) - H_{o,i} + \sum_j \left[\left(\dfrac{1}{\varepsilon_{rad,j}} - 1 \right) F_{i-j} q_{rad,j} \right] \right\}$	(19)
View Factor	$F_{i-j} = \dfrac{\cos(\theta_i) \cos(\theta_j)}{\pi r^2} dA_j$	(20)

Table 5: Radiation model equations
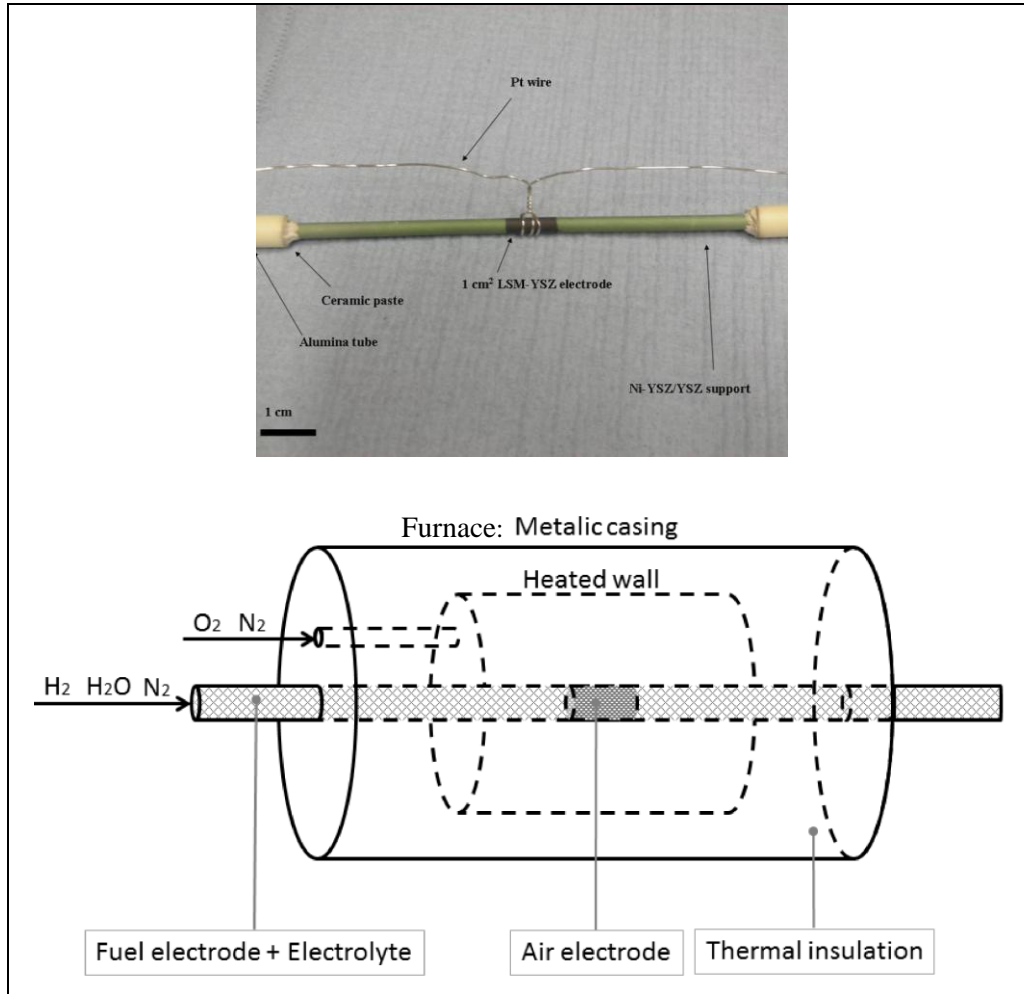
2. Numerical Simulations

Figure 2: Picture of the microtubular SORFC [2] on the top and sketch of the test rig on the bottom.

Numerical simulations reproducing the experimental test rig shown in Figure 2 (bottom) were carried out considering the following five adjacent numerical subdomains: (i) "Fuel channel" represents the void space inside the electrode-electrolyte tube, it is a 10 cm long cylindrical channel; (ii) "Fuel electrode" represents the 10 cm long porous hollow tube of Ni-YSZ; (iii) "Electrolyte" domain stands for the impervious hollow tube made of YSZ; (iv) "Air electrode" is about 1 cm long porous hollow tube made of LSM-YSZ (active area of 1 cm^2); and "Air channel" represents the void space between the SORFC and the heated wall of the furnace.

On the experimental side, the reversible operation of the cell has been successfully tested for different fuel compositions and the results are reported in [2]. In this work the reference experimental data set is that reported in [2] for 70% steam concentration in the fuel stream (i.e. 15 % H_2, 70 % H_2O, 15 % N_2).

The numerical and experimental J-V curves of the reversible solid oxide cell operating at the reference conditions are shown in Figure 1; numerical results agree with experimental data.

Further numerical results are presented and analysed below.

3. Results

A numerical tool such the one developed by the authors does not only provide J-V curves that allow the prediction of the cell global performance. It also provides a wide range of interesting results that may be even more useful for experimentalist than the prediction of j-V curve itself. A selection of these complementary results is presented and analysed in this section.

The microstructure of the porous electrodes is closely related to the species mass transfer to the reaction sites, which is essential to avoid fuel depletion in the triple phase boundaries and the corresponding failure in performance. In Figure 3, Figure 4 and Figure 5 the reactants and products concentrations along the electrodes-electrolyte interfaces (i.e. reacting walls) are shown for both operating modes at different cell voltages.

Figure 3 shows the hydrogen molar fraction along the fuel electrode for SOEC and SOFC modes, the analysis of the latter being of interest. In SOFC mode, hydrogen concentration remains constant from the inlet (x=0) to the air electrode position (4.5 cm). Hydrogen is then consumed within a distance of about 1 cm (air electrode length) and then it reaches a concentration, lower that the feeding one, that remains constant until the electrode end (x=10cm). For low voltages, it can be seen how hydrogen is about to be depleted within the 1cm long reactive area, despite the fact that the hydrogen at the end of the electrode is far from depleted. Moreover, significant concentration differences along the reactive wall may be found for low voltages.

Figure 4 shows the H_2O concentration distribution along the fuel electrode. As pointed out in Figure 3, the species is consumed (SOFC) or produced (SOEC) only in the central area of the fuel electrode, corresponding to the position of the air electrode. Most interesting results are those for the SOEC mode, where it can be observed how the concentration of H_2O decreases in the active area to lower values than that found at the electrode outlet, and steep concentration gradients are found for high operating voltages.

From the above analysis of Figure 3 and Figure 4, it can be stated that mass transfer within the fuel electrode is strongly impeded both in SOFC and SOEC modes when operating the cell at high current densities. This indicates that a modification on the fuel electrode microstructure such as an increase of the porous diameter or the porosity could improve the cell performance.

Likewise Figure 5 shows the oxygen molar fraction along the air electrode for both SOEC and SOFC modes and several operating voltages. The oxygen distribution in both operating modes and for any voltage remains almost flat, indicating that mass transport of oxygen is not as critical as in the fuel electrode. Thus, the air electrode microstructure should not be a matter of concern for such a thin air electrode.
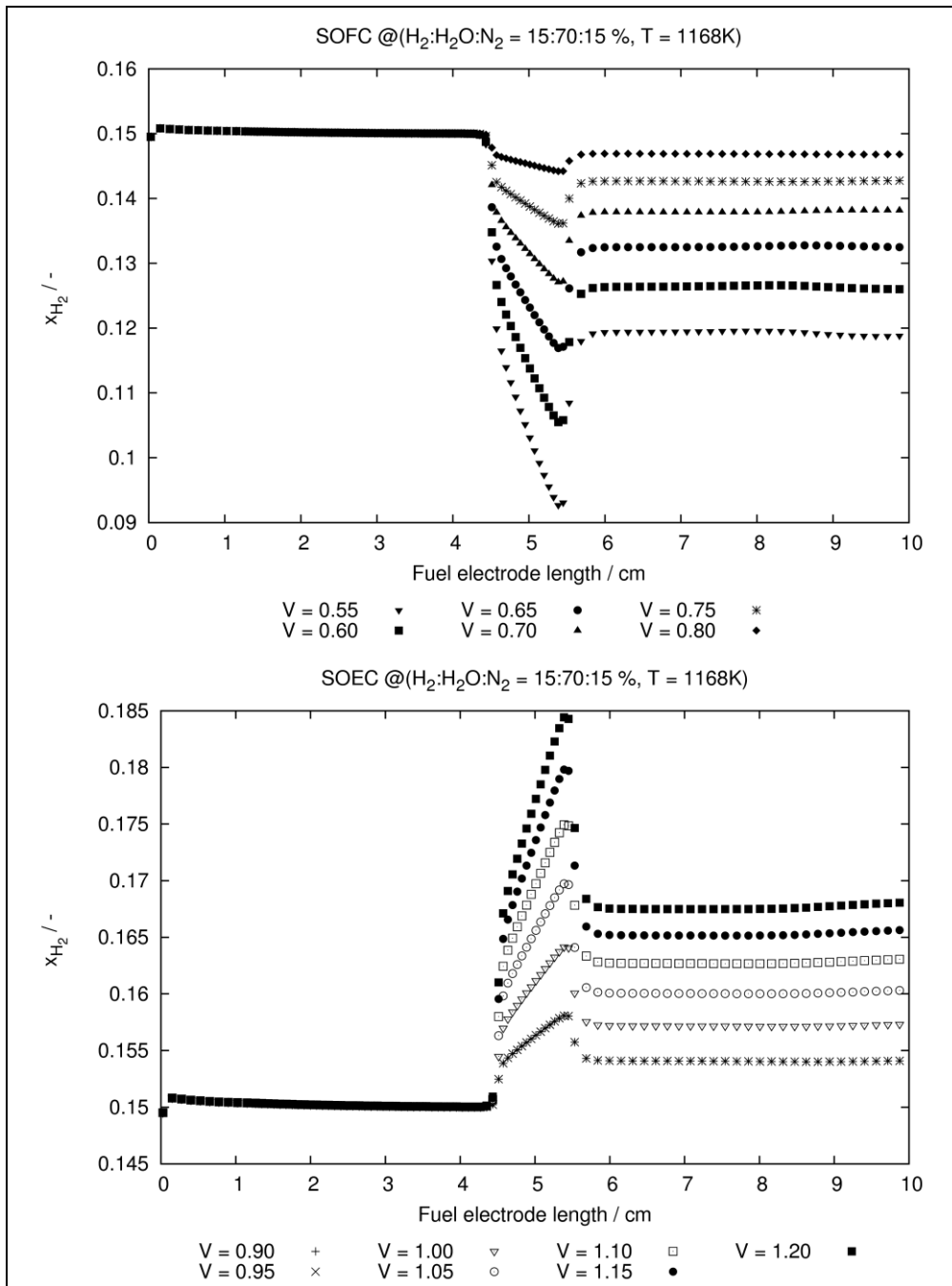
Figure 3: Numerical H_2 molar-fraction distribution along the reaction wall of the fuel electrode for SOFC and SOEC modes at different operating voltages
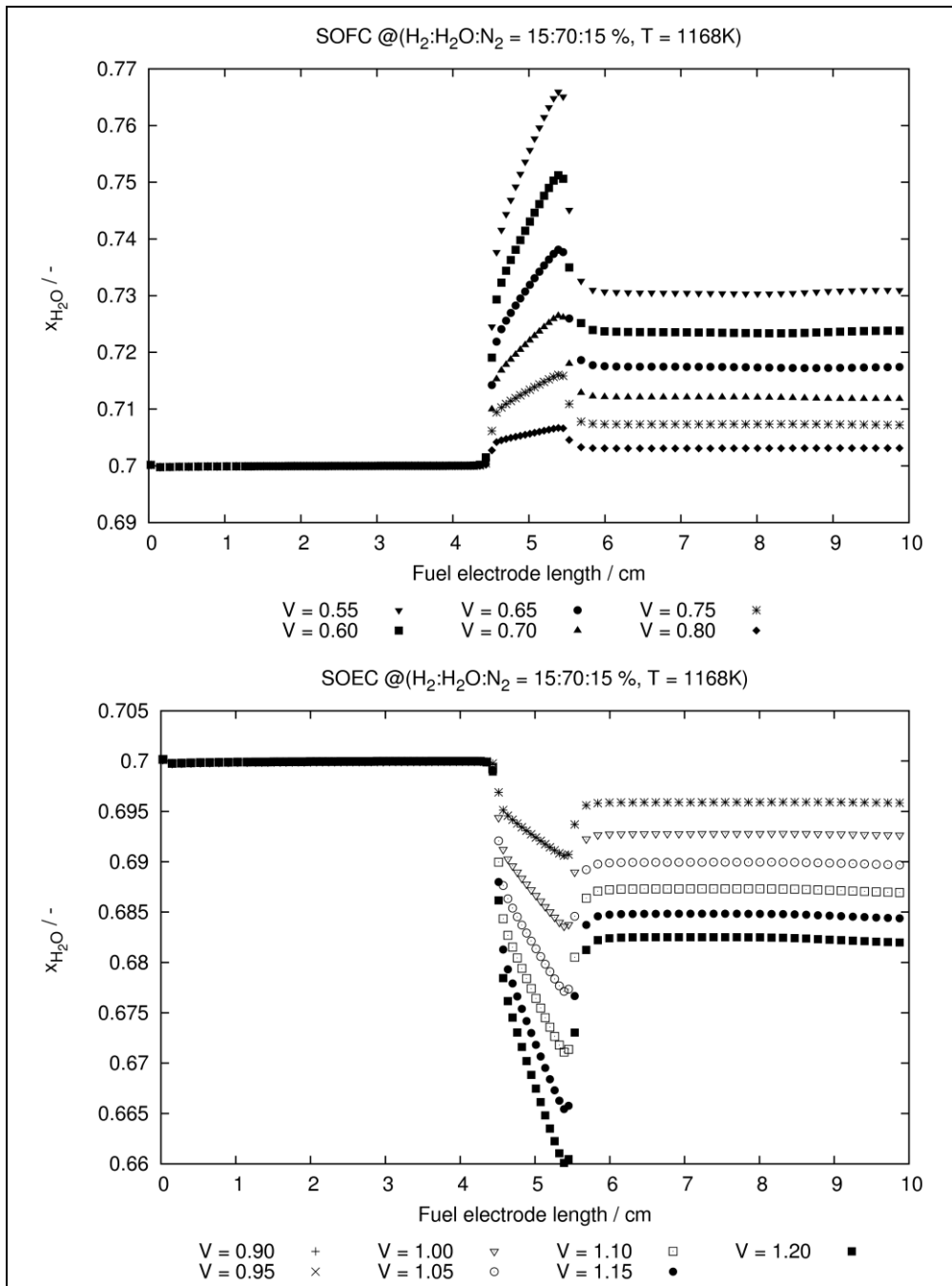
Figure 4: Numerical H2O molar-fraction distribution along the reaction wall of the fuel electrode for SOFC and SOEC modes at different operating voltages
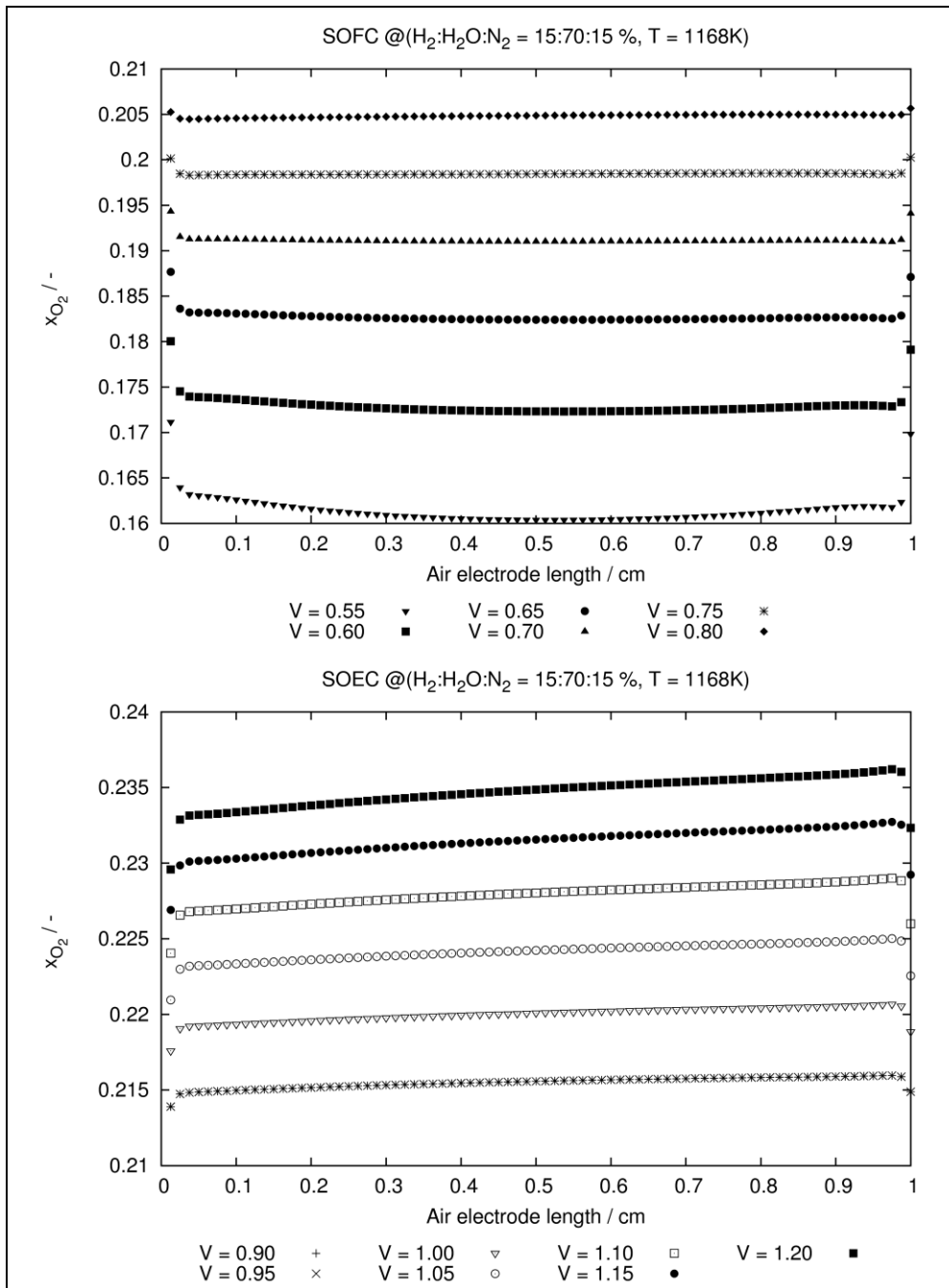
Figure 5: Numerical O2 molar-fraction distribution along the reaction wall of the air electrode for SOFC and SOEC modes at different operating voltages

Other interesting information that can be extracted from the numerical simulations is the temperature distribution inside the cell. Figure 6 shows the temperature distribution along the air electrode for both operating modes and for the given operating voltages. Here, the study of the different thermal behavior between the direct and reverse operating modes is of relevance. In the SOFC mode the predicted? cell temperature is on average close to the measured temperature (T_{setup}), while in SOEC mode the predicted? cell temperature is at any case lower than the measured one. Additionally, it is clear that the SOFC temperature increases as the cell voltage is decreased (i.e the current density is increased). In the SOEC mode temperature decreases as the current density is increased (higher voltages) due to the endothermic nature of the reverse reaction. However, at a given point the temperature starts increasing if the current density (i.e. the voltage) is further increased. This indicates that Joule heating together with radiation heat transfer can balance and even exceed the heat sink due to the electrochemical reaction. This is an interesting result that must be considered for a deeper study of the thermally self-sustaining SOEC operation.

References

[1]   García-Camprubí, M., Jasak, H., Fueyo, N. Journal of Power Sources, 196 (17), 7290-7301, 2011.
[2]   Laguna-Bercero, M.A., Campana, R., Larrea, A., Kilner, J.A., Orera, V.M. Journal of the Electrochemical Society, 157 (6), B852-B855, 2010.
[3]   García-Camprubí, M., Fueyo, N. Journal of Power Sources, *Submitted,* 2012.
[4]   Jensen, S. H., Sun, X., Ebbesen, S. D., Knibbe, R., Mogensen M. International Journal of Hydrogen Energy, 35 (18), 9544 – 9549, 2010.
[5]   Hashimoto, S., Liu, Y., Mori, M., Funahashi, Y., Fujishiro, Y. International Journal of Hydrogen Energy 34 (3), 1159 – 1165, 2009.
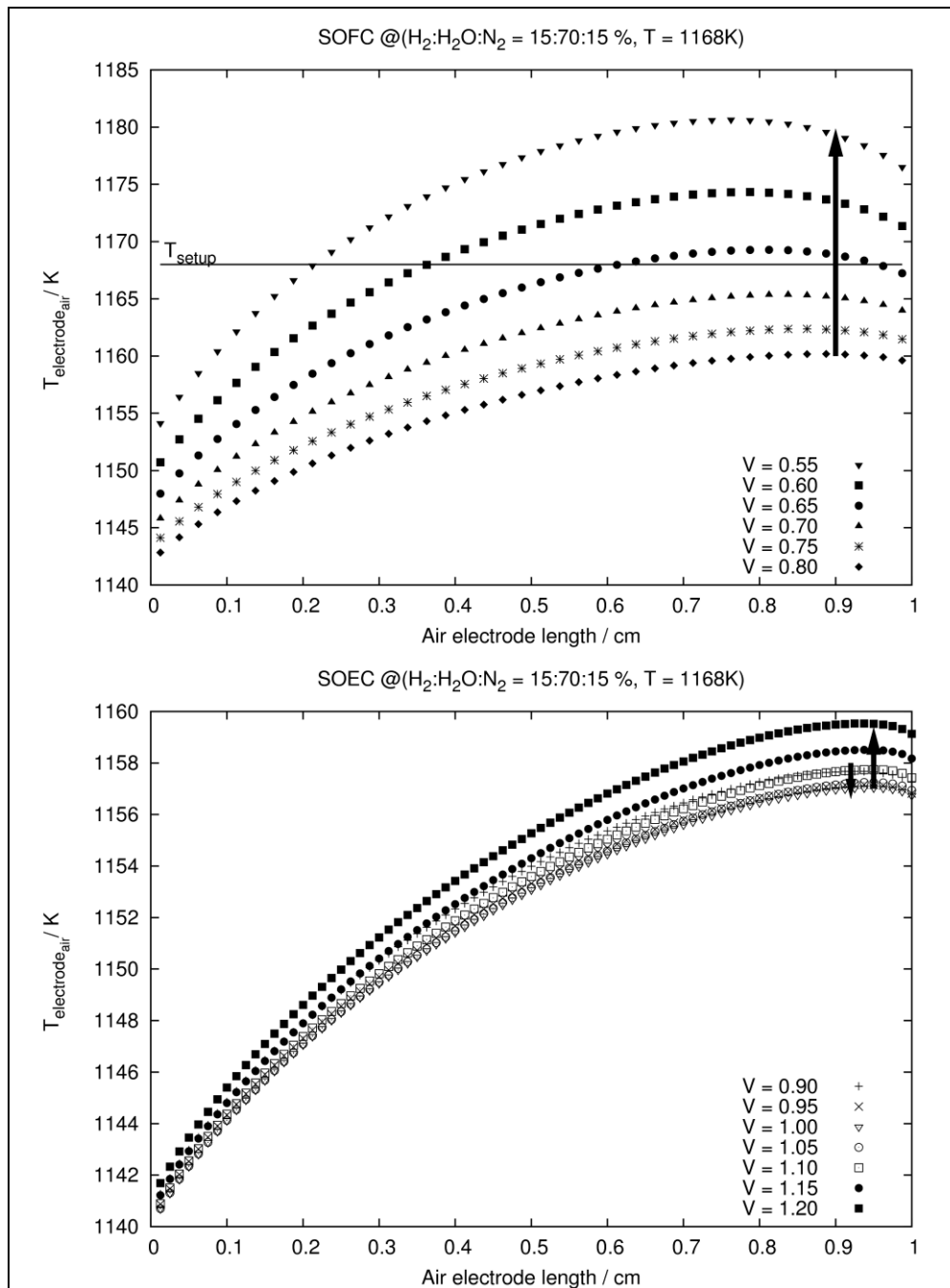[6]   Jin, X., Xue, X. Journal of Power Sources 195 (19) 6652 – 6658, 2010.

Figure 6: Numerical temperature distribution along the reaction wall of the air electrode, for SOFC and SOEC modes at different operating voltages

Nomenclature

B_o	Permeability of the porous-medium, m^2
C_p	Specific heat at constant pressure of the fluid, $m^2\ s^{-2}\ K^{-1}$
$D_{\alpha m}$	Diffusion coefficient of species α in the gas mixture, $m^2\ s^{-1}$
E^o	Standard electrochemical cell voltage, V
E_b	Blackbody emissive power, $kg\ s^{-3}$
F	Faraday's constant, $A\ s\ kmol^{-1}$
F_{i-j}	View factor between surface i and surface j, -'
h	Sensible enthalpy of the fluid, $m^2\ s^{-2}$
h_α	Sensible enthalpy of the species α in the fluid , $m^2\ s^{-2}$
H_o	External radiation , $kg\ s^{-3}$
i	Current density, $A\ m^{-2}$
i_o	Exchange current density, $A\ m^{-2}$
$\vec{j}_\alpha$	Mass diffusive flux of species α , $kg\ m^{-2}\ s^{-1}$
k_B	Boltzmann's constant, $kg\ m^2\ s^{-2}\ K^{-1}$
n	Number of electrons to convert a single molecule of species α , -
$\vec{n}$	Normal unit-vector, -
$\vec{N}_\alpha$	Total molar flux of species α , $kmol\ m^{-2}\ s^{-1}$
p	Pressure, $kg\ m^{-1}\ s^{-2}$
p_α	Partial pressure of species α , $kg\ m^{-1}\ s^{-2}$
$\vec{q}$	Energy flux, $kg\ s^{-3}$
Q	Volumetric heat sources, Joule heat, $kg\ m^{-1}\ s^{-3}$
$\vec{r}$	Vector from channel surface to enclosure, m
R	Ideal gas constant, $kg\ m^2\ s^{-2}\ kmol^{-1}\ K^{-1}$
S_α	Volumetric molar source of species α , $kmol\ m^{-3}\ s^{-1}$
T	Temperature, K
$\vec{v}$	Fluid velocity, $m\ s^{-1}$
V	Voltage, V
W_α	Molecular weight of species α , $kg\ kmol^{-1}$
x_α	Molar fraction of species α in the gas mixture, -
y_α	Mass fraction of the species α , -

Greek Symbols

α	Gas mixture species, -

$\bar{\alpha}$	Backward transfer coefficient, -
$\vec{\alpha}$	Forward transfer coefficient, -
β	Gas mixture species, -
γ	Pre-exponential coefficient, $A\ m^{-2}$
Γ_α^*	Dusty-gas model parameter, $m^2\ s^{-1}$
ε	Porosity, -
ε_{rad}	Emissivity of the surface, -
η	Overpotential, V
θ	Angle, -
λ	Thermal conductivity of the fluid, $kg\ m\ s^{-3}\ K^1$
λ_s	Thermal conductivity of the solid, $kg\ m\ s^{-3}\ K^1$
λ^{eff}	Effective thermal conductivity of the fluid and porous medium as a continuum, $kg\ m\ s^{-3}\ K^1$
μ	Viscosity of the fluid, $kg\ m^{-1}\ s^{-1}$
μ_α	Viscosity of species α, $kg\ m^{-1}\ s^{-1}$
ρ	Fluid density, $kg\ m^3$
σ	Anionic conductivity, $A\ V^1\ m^{-1}$
τ	Tortuosity factor, -
$\vec{\upsilon}_\alpha^{p*}$	Dusty-gas model parameter, $m\ s^{-1}$
$\vec{\upsilon}_\alpha^{N*}$	Dusty-gas model parameter, $m\ s^{-1}$
ϖ	Heat of reaction, $kg\ m^{-1}\ s^{-3}$

Subscripts

a	Fuel electrode
act	Activation
c	Air electrode
con	Concentration
e	Electrolyte
$fuel$	Fuel
i	Index of surface element, -
j	Index of surface element, -
ocv	Open circuit voltage
ohm	Ohmic
rad	Radiation
ref	Reference
rw	Reaction wall, active electrode-electrolyte interface